

## Aerodynamic Noise Computation of the Flow Field around NACA 0012 Airfoil Using Large Eddy Simulation and Acoustic Analogy

M. Ghasemian and A. Nejat\*

*Department of Mechanical Engineering, University of Tehran, Tehran, Iran*

Received 10 January 2015; Accepted 25 February 2015

### Abstract

The current study presents the results of the aerodynamic noise prediction of the flow field around a NACA 0012 airfoil at a chord-based Reynolds number of 100,000 and at 8.4 degree angle of attack. An incompressible Large Eddy Simulation (LES) turbulence model is applied to obtain the instantaneous turbulent flow field. The noise prediction is performed by the Ffowcs Williams and Hawkins (FW-H) acoustic analogy. Both mean flow quantities and fluctuation statistics are studied. The behaviour of the turbulent vortical structures in the flow field from the perspective of the turbulent boundary layer development is visualized. Power spectral density of the lift coefficient is presented. The computed non-dimensional mean velocity profiles in the boundary layer compared reasonably well with the theoretical predictions. The boundary layer transition from a laminar state to a turbulent state is also brought into focus. The skin friction coefficient and the  $u_{rms}$  streamwise velocity fluctuations predicted a transition zone from  $x/c=0.23$  to  $x/c=0.45$ . Then, the research focuses on the broadband noises of the turbulent boundary layers and the tonal noises that arise from the vortex shedding generated by the laminar boundary layers. The spectra computed from the acoustic pressure are compared with the experimental data. The effect of observer location on the overall sound pressure level (OASPL) is investigated and the results indicate that the OASPL varies logarithmically with the receiver distance, as was expected.

**Keywords:** *acoustic analogy, aerodynamic noise, boundary layer transition, turbulence.*

### 1. Introduction

Aerodynamic noise generated by wind turbines may cause annoyance for people living in the vicinity of the wind turbines [1, 2]. Aerodynamic noise radiating from the blades is mainly associated with the interaction of turbulence with the blade surface [3]. Therefore, it is important to identify and

predict the most important aerodynamic noise sources. It is found [4] that flow-induced noise is the most important contributor in the noise generation mechanism of wind turbines. This noise arises from the interaction between an airfoil blade and the turbulence produced in its own boundary layer and near wake. Flow-induced noise could be classified as discrete frequency (tonal) noise and broadband noise in character. According to [5], airfoil self-noises

---

\* Corresponding Author, Tel.: +98 21 82084813; Fax: +98 21 88013029, Email: nejat@ut.ac.ir

can be divided into five types: turbulent boundary layer-trailing edge noise; laminar boundary layer-vortex shedding noise; separation-stall noise; trailing edge bluntness-vortex shedding noise; and tip vortex shedding noise

Traditionally, noise prediction methods have used empirical or semi-empirical considerations. In recent years, the interest in the computational acoustics has increased. Numerical simulation of airfoil noise is a relatively new research topic. Wang and Moin [6] carried out an incompressible large eddy simulation for turbulent boundary layer flow around an asymmetrically bevelled trailing edge of a flat strut. The far-field acoustic is computed by the acoustic analogy of Ffowcs Williams and Hall [7]. Singer et al. [8] solved the Reynolds-Averaged Navier–Stokes (RANS) equations and the Ffowcs Williams and Hawkins (FW-H) acoustic analogy to investigate the sound generated by a bluff-body vortex generator positioned close to the sharp trailing edge of a two-dimensional airfoil. Shen et al. [9] used the flow acoustics splitting technique to compute the aero-acoustic of the flow field around a NACA 0015 airfoil at  $Re=1.6 \times 10^5$  for different angles of attack. They used large eddy simulation to obtain the instantaneous flow quantities. A parametric study of the noise pattern for different angles of attack shows that the noise level increases with the increment of angles of attack. Jones et al. [10] conducted Direct Numerical Simulations of the flow over NACA 0006 and NACA 0012 airfoils. Their results show that the contribution of trailing edge noise radiation is significant for low frequencies, while for the high frequencies, the radiated noise appears to be due only to flow events in the transition/reattachment region on the suction side. The aerodynamic and acoustic optimization process of decreasing the noise emission levels while increasing the aerodynamic performance can be found in studies conducted by Kim et al. [11] and Göçmen et al. [12]. Their results show that redesigned airfoils have lower levels of noise emission and higher lift-to-drag ratios. Recently, Wolf and Lele [13] studied the generation and propagation of broadband and tonal noise for different flow conditions over a NACA 0012 airfoil.

The present investigation addresses some

aspects of the boundary layer transition and its effects on the sound pressure spectra which are not covered in the literature. The turbulent vortical structures in the boundary layer development are studied, which were not fully understood in the previous publications.

The current study predicts the aerodynamic noise from the flow field around a NACA 0012 airfoil at  $Re= 100,000$  and  $AoA= 8.4deg$ . Incompressible LES is conducted to obtain the instantaneous turbulent flow field. The noise predictions are performed by the FW-H acoustic analogy. This study focuses on the transition phenomena in the boundary layer. Both mean flow quantities and fluctuation statistics are studied, and the power spectral density of lift coefficient and far-field sound pressure level plots are presented. The sound pressure spectra are compared with the experimental data of Brooks et al. [5].

## 2. Governing Equations

### 2.1. LES formulation

The three-dimensional unsteady incompressible Navier-Stokes equations have been solved by the LES technique. In the LES approach, it is recognized that the large turbulent structures are generally much more energetic than the smaller scales; thus these large structures are resolved, while scales smaller than the size of the computational mesh are modelled.

The equations are written in conservation form as:

$$\frac{\partial \bar{u}_i}{\partial x_i} = 0 \quad (1)$$

$$\frac{\partial}{\partial t} \bar{u}_i + \frac{\partial}{\partial x_j} (\bar{u}_i \bar{u}_j) = -\frac{1}{\rho} \frac{\partial \bar{p}}{\partial x_i} + \frac{1}{\rho} \frac{\partial \tau_{ij}^R}{\partial x_j} + \nu \nabla^2 \bar{u}_i \quad (2)$$

where  $\bar{u}_i$  and  $\bar{p}$  denote resolved velocity components and pressure, respectively. The influence of the unresolved scales is incorporated in the subgrid stress tensor, which includes the residual stresses,  $\tau_{ij}^R$ , defined as:

$$\tau_{ij}^R = \rho (\overline{u_j u_j} - \bar{u}_i \bar{u}_j) \quad (3)$$

The subgrid scale stresses resulting from the filtering operation are unknown and require modelling. The dynamic subgrid model formulation of Lilly [14] is used to include the effects of unresolved turbulent scales.

## 2.2. Aeroacoustic formulation

In the present study, the Ffowcs Williams and Hawkings (FW-H) method [15] is used to predict the far-field noise. The FW-H equation is the most general form of the Lighthill acoustic analogy [16] and is appropriate for the prediction of sound generated by rigid bodies in arbitrary motion. The FW-H equation is an inhomogeneous wave equation that can be derived by manipulating the continuity equation and the Navier-Stokes equations. The FW-H equation can be written [17, 18] as:

$$\frac{1}{a_0^2} \frac{\partial^2 p'}{\partial t^2} - \nabla^2 p' = \frac{\partial^2}{\partial x_i \partial x_j} \{T_{ij} H(f)\} - \frac{\partial}{\partial x_i} \{[P_{ij} n_j + \rho u_i (u_n - v_n)] \delta(f)\} + \frac{\partial}{\partial t} \{[\rho_0 v_n + \rho (u_n - v_n)] \delta(f)\} \quad (4)$$

where  $u_n$  is the fluid velocity in the direction normal to the integration surface,  $v_n$  is the normal velocity of the integration surface,  $\delta(f)$  is Dirac delta function and  $H(f)$  is Heaviside function. Subscript  $_0$  defines the value in undisturbed medium and the primed value represents the difference between the value in real state and in undisturbed medium (e.g.,  $p' = p - p_0$ ).

The shape and the motion of the control surface is defined by  $f(\vec{x}, t) = 0$ , with  $f < 0$  for its interior and  $f > 0$  for its exterior.

The terms on the right-hand side of Equation (4) refer to different mechanisms of sound production. The first source term involves Lighthill stress tensor and shows that the time-dependent stresses, including momentum, viscosity and turbulence, generate sound. Such sources are called quadrupoles. The Lighthill stress tensor is defined as:

$$T_{ij} = \rho u_i u_j + P_{ij} - a_0^2 (\rho - \rho_0) \delta_{ij} \quad (5)$$

where  $P_{ij}$  is the compressive stress tensor that includes the surface pressure and viscous stress.

The second term involves the external forces called dipoles or loading noise. The last source term involves the mass flow rate called monopole or thickness noise.

Thickness and loading terms are surface distribution sources, as indicated by the

presence of the delta function ( $f$ ), while the quadrupole term is a volume distribution of sources indicated by Heaviside function  $H(f)$ . The wave Equation (4) can be integrated analytically under the assumptions of the free-space flow and the absence of obstacles between the sound sources and the receivers. The complete solution consists of surface integrals and volume integrals. The surface integrals represent the contributions of monopole and dipole acoustic sources and partially of quadrupole sources, whereas the volume integrals represent quadrupole (volume) sources in the region outside the source surface. The contribution of the volume integrals becomes small when the flow is low subsonic, and the source surface encloses the source region and can be neglected. Thus, acoustic pressure  $p'$  which is mentioned in Equations (4) is composed as follows:

$$p'(\vec{x}, t) = p'_T(\vec{x}, t) + p'_L(\vec{x}, t) \quad (6)$$

where  $\vec{x}$  is the observer position,  $t$  is the observer time, and the subscripts T and L correspond to thickness (monopole) and loading (dipole) components, respectively [19]:

$$4\pi p'_T(\vec{x}, t) = \int_{f=0} \left[ \frac{\rho_0 (\dot{U}_n + U_{\dot{n}})}{r(1-M_r)^2} \right]_{ret} dS + \int_{f=0} \left[ \frac{\rho_0 U_n (r\dot{M}_r + a_0(M_r + M^2))}{r^2(1-M_r)^3} \right]_{ret} dS \quad (7)$$

and

$$4\pi p'_L(\vec{x}, t) = \frac{1}{a_0} \int_{f=0} \left[ \frac{\dot{L}_r}{r(1-M_r)^2} \right]_{ret} dS + \int_{f=0} \left[ \frac{L_r - L_M}{r^2(1-M_r)^3} \right]_{ret} dS + \frac{1}{a_0} \int_{f=0} \left[ L_r \frac{(r\dot{M}_r + a_0(M_r + M^2))}{r^2(1-M_r)^3} \right]_{ret} dS \quad (8)$$

where

$$U_i = v_i + \frac{\rho}{\rho_0} (u_i - v_i) \quad (9a)$$

$$L_i = P_{ij} \hat{n}_j + \rho u_i (u_n - v_n) \quad (9b)$$

The various subscripted quantities appearing in (7) and (8) are the inner products of a vector and a unit vector implied by the subscript. For instance,  $L_r = \vec{L} \cdot \vec{r}$  and  $U_n =$

$\vec{U} \cdot \vec{n}$  where  $\vec{r}$  and  $\vec{n}$  denote the unit vectors in the radiation and wall-normal directions, respectively. The dot over a variable denotes source-time differentiation of that variable. The Mach number vector  $M_i$  is the local surface velocity vector divided by the freestream sound speed. The subscript *ret* denotes that the integrand is evaluated at the retarded time,  $\tau$ , defined as:

$$\tau = t - \frac{r}{a_0} \quad (10)$$

where  $t$ ,  $r$  and  $a_0$  are receiver time, the distance to the receiver and the speed of sound, respectively.

### 3. Problem Description

This study is carried out on a NACA 0012 airfoil section. A three-dimensional unsteady computational fluid dynamics solver, Ansys Fluent 14.5, based on the finite volume method, is employed to solve the Navier-Stokes equations using LES technique. The fluid is assumed to be incompressible as the freestream Mach number is low ( $M=0.093$ ). Due to the incompressibility of the flow, the pressure-based solver, which is traditionally implemented to solve low-speed incompressible flows, is chosen. The PISO algorithm is chosen to couple the velocity-pressure equations. Spatial discretization is achieved using second-order central differences.

An O-type hexahedral grid with element number of  $231 \times 151 \times 27$  was used in this study. The spanwise width is  $L_z = 0.1C$ , and the grid distribution along the airfoil span is uniform. Special attention is given to minimizing mesh non-orthogonality and skewness. A good mesh quality is necessary to obtain accurate results and to reduce the computational time.

The height of the first row of cells bounding the airfoil is set to be  $10^{-5}C$  which ensures  $y^+ < 1$  for cells immediately adjacent to the airfoil. Figure 1 shows  $y^+$  over both the airfoil suction and pressure sides for  $Re=10^5$  and  $AoA = 8.4$  deg.

As Figure 1 shows, the boundary layer can be properly resolved without using a wall function. The domain extends up to 12.5 chord lengths in the transverse direction. Periodic boundary condition is used in the spanwise direction.

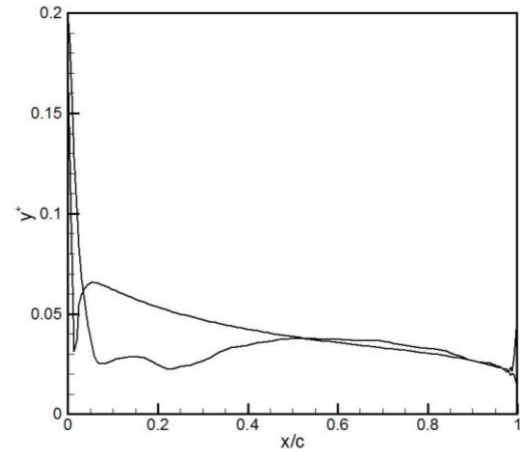


Fig. 1. Distribution of  $y^+$  along the NACA 0012 airfoil at  $AoA=8.4$  deg. and  $Re=10^5$

The numerical time-step size is set to be  $10^{-5}$ s. Computation is initialized with converged RANS  $k-\omega$ SST results on the same grid. The calculation runs for approximately 45 characteristic flow times and the statistics are collected over the last 20 time units.

### 4. Results and Discussion

#### 4.1. Aerodynamic results

The pressure coefficient of the airfoil in terms of aerodynamic characteristics and boundary layer behaviour is an important parameter. This distribution along the airfoil chord is shown in Figure 2. To validate the CFD results, the pressure coefficient obtained from LES is compared with the Xfoil data. The comparison shows the accuracy of the LES results. It can be observed that the boundary layer is approximately subjected to an adverse pressure gradient on the whole airfoil suction side.

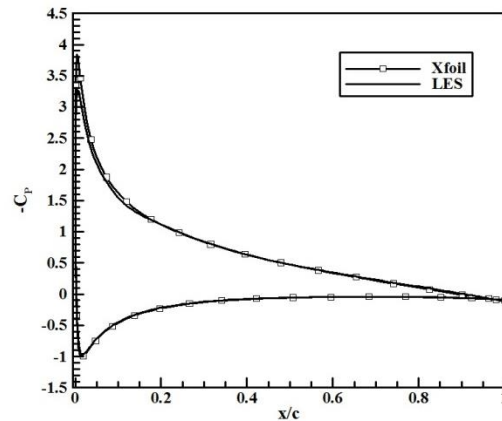


Fig. 2. The distribution along the airfoil chord

The lift history was recorded for this study. Figure 3 shows the instantaneous lift coefficient vs. the airfoil's characteristic flow time. It can be seen that the instantaneous lift coefficient fluctuates around the mean lift coefficient ( $C_{l,mean} = 0.829$ ). Sheldahl et al. [20] obtained  $C_{l,mean} = 0.827$  for the same condition. The comparison shows the accuracy of this LES computation.

Power spectral density of the lift coefficient is shown in Figure 4. It can be observed that the fluctuation magnitude is extremely low. However, several features are detected from data. First, there are tonal peaks due to vortex shedding in the laminar boundary layer. Second, there is relatively large fluctuation near the frequency of  $f = 2000\text{Hz}$  related to a Strouhal number of  $St = 3.2$ . Third, with increase in the frequency from left to right, the energy content decreases; this point means that the energy content in the flow is decreasing from larger to smaller structures.

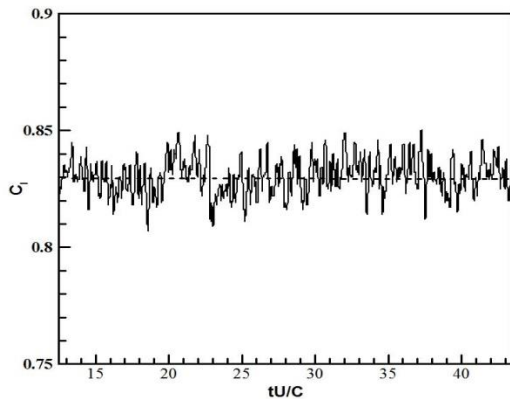


Fig. 3. Time history of the instantaneous and mean lift coefficient

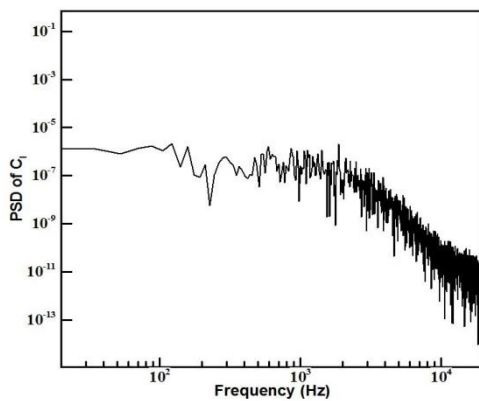


Fig. 4. Power spectral density of lift coefficient

The non-dimensional mean streamwise velocity profile at  $x/c=0.1$  and  $x/c=0.5$  in the mid-span plane is compared with the theoretical predictions, as showed in Figure 5. Non-dimensional velocity  $u^+$  and non-dimensional length  $y^+$  are defined as below:

$$u^+ = \frac{u}{u_\tau}, \quad y^+ = \frac{yu_\tau}{\nu} \quad (11)$$

where  $u_\tau = \sqrt{\frac{\tau_w}{\rho}}$  is friction velocity at the wall. This scaling takes into account the wall shear stresses. Typical laminar boundary layer behaviour is observed at  $x/c=0.1$ , where  $u^+ = y^+$  over the viscous sublayer thickness. The velocity profile at  $x/c=0.5$  shows a viscous sublayer behaviour until approximately  $y^+ = 10$ . From  $y^+ = 10$  to around  $y^+ = 100$ , the profile deviates from the standard logarithmic law  $u^+ = 2.44 \ln y^+ + 5.2$  established for a zero pressure gradient boundary layer. Due to the adverse pressure gradient, the velocity profile at  $x/c=0.5$  is compared with Afzal's [21] approach, which takes into account the adverse pressure gradient effects.

$$u^+ = 2.44 \left( \ln y^+ - 2 \ln \frac{\sqrt{1 + \lambda y^+} + 1}{2} + 2(\sqrt{1 + \lambda y^+} - 1) \right) + 5.2 \quad (12)$$

where

$$\lambda = \left( \frac{u_p}{u_\tau} \right)^3, \quad u_p = \left( \frac{\nu}{\rho} \frac{dp}{dx} \right)^{\frac{1}{3}} \quad (13)$$

As Figure 5 shows, velocity profile at  $x/c=0.5$  represents better fit with this approach.

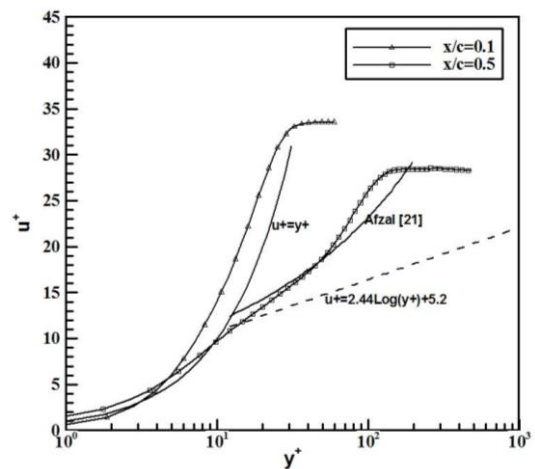


Fig. 5. Velocity profiles on upper side of the airfoil

Figures 6(a-b) indicates the instantaneous velocity magnitude and normal component. It can be seen from the y-velocity contour that circulation bubbles are created along the suction side of the airfoil.

Due to the relatively high angle of attack, there is a possibility of separation on the airfoil suction side. Flow circulation and separation around the airfoil suction side are shown in Figures 7(a-b). It can be seen that there is a small circulation zone in  $\frac{x}{c} = 0.2$  at the upper side of the airfoil.

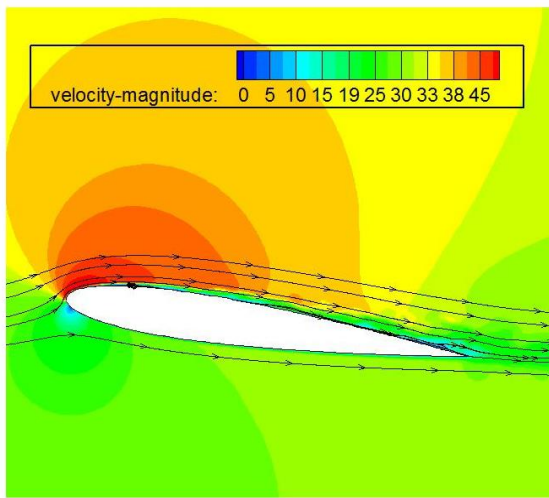


Fig. 6. a) contour of instantaneous magnitude velocity

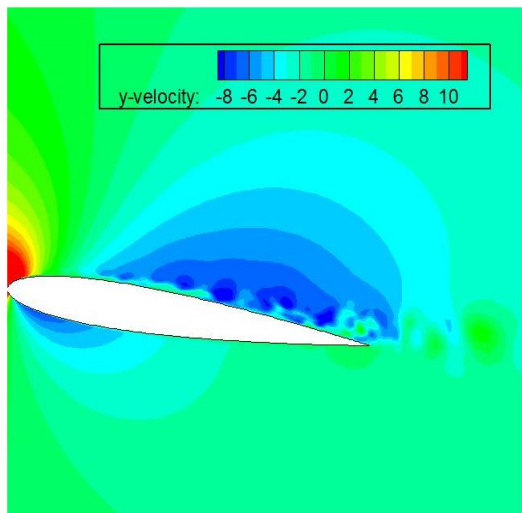


Fig. 6. b) Contour of instantaneous y-velocity

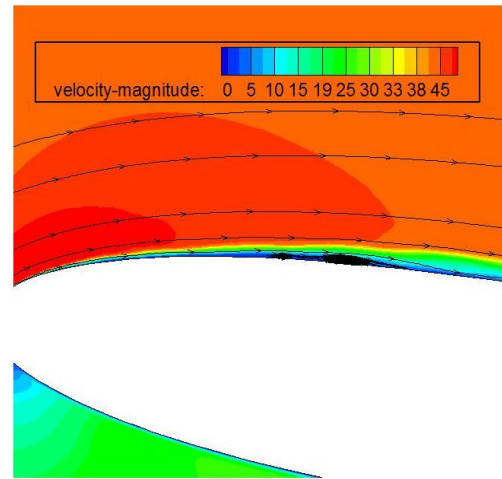


Fig. 7. a) Streamline and circulation zone on the suction side of the airfoil

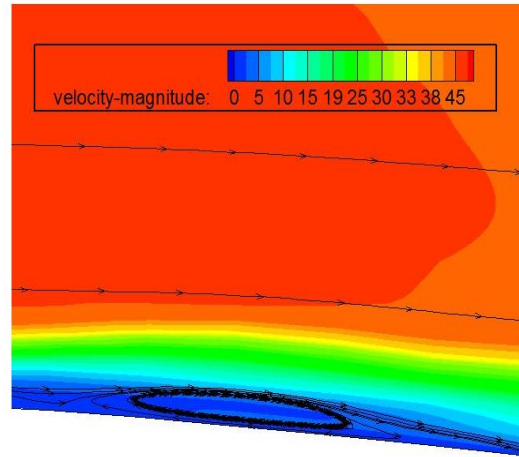


Fig. 7. b) Magnified circulation zone on the suction side of the airfoil

Figure 8 shows the skin friction coefficient distribution along the airfoil suction side. It can be seen that a large laminar region is not presented, and the skin friction reaches its minimum around  $x/c=0.23$ . Then, it rises rapidly to a peak at about  $x/c=0.45$ . This behaviour of the skin friction coefficient shows a transition region from  $x/c=0.23$  to  $x/c=0.45$  corresponding to  $Re= 23,000$  and  $Re= 45,000$ , respectively. These low Reynolds numbers are probably due to the angle of attack and turbulence intensity in the inflow condition. It should be noted that transition is very sensitive to different flow parameters [22, 23].

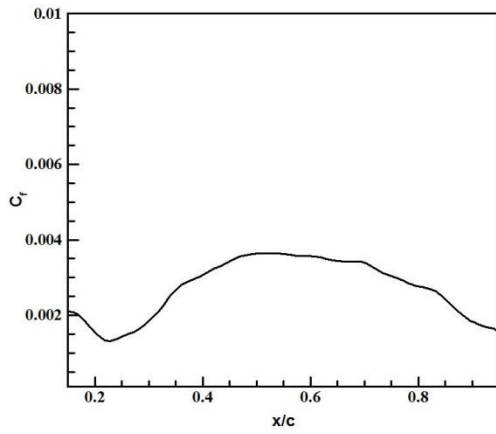


Fig. 8. Skin friction coefficient along the upper side of airfoil

Figure 9 shows the turbulent velocity fluctuations calculated at  $y^+=50$  along the airfoil suction side. The magnitude of  $u_{rms}$  begins to increase rapidly from  $x/c=0.2$ , and then it reaches to 20% of the freestream velocity at  $x/c=0.37$ . This level is approximately constant until  $x/c=0.5$  and then commences to decrease until the trailing edge. It can be concluded that there is a transition zone from  $x/c=0.2$  to  $x/c=0.5$ . These values are in good agreement with values obtained from the skin friction coefficient.

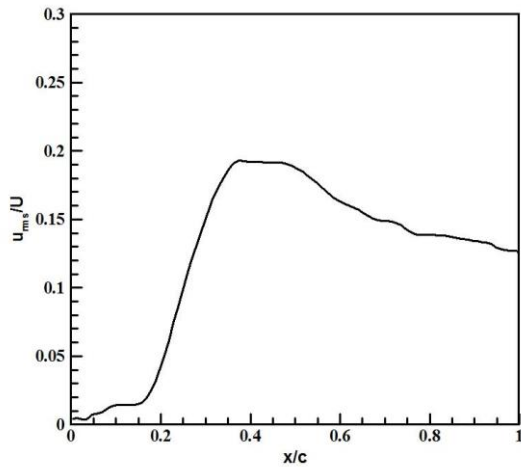


Fig. 9. Velocity fluctuations  $u_{rms}/U$  in the upper boundary layer

Turbulent vortical structures of the flow field are visualized in Figures 10(a-c). To identify these vortex structures, the Q-criterion isosurface coloured with the streamwise velocity is used. The Q-criterion, which is the second invariant of the velocity gradient tensor, is defined as below [24, 25]:

$$Q = \frac{1}{2}(\Omega_{ij}\Omega_{ij} - S_{ij}S_{ij}) \quad (14)$$

where

$$S_{ij} = \frac{1}{2}\left(\frac{\partial u_i}{\partial x_j} + \frac{\partial u_j}{\partial x_i}\right), \quad \Omega_{ij} = \frac{1}{2}\left(\frac{\partial u_i}{\partial x_j} - \frac{\partial u_j}{\partial x_i}\right) \quad (15)$$

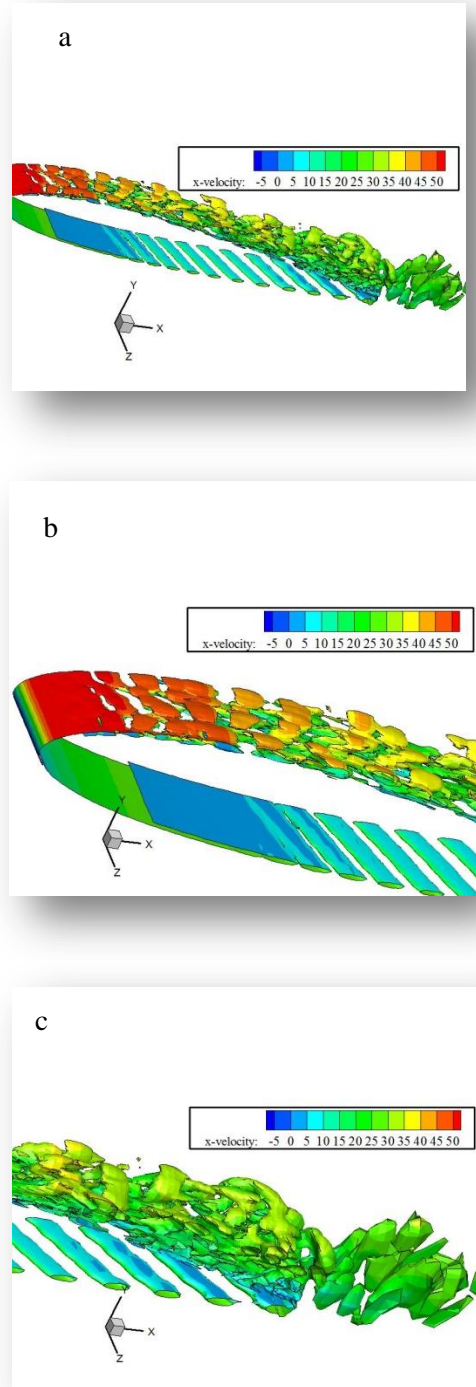


Fig. 10. Isosurface of turbulent vertical structures for  $Q=2*107s-2$  contoured by streamwise velocity. a) Whole suction side, b) Leading edge, c) Trailing edge

It can be observed that turbulent structures are aligned in spanwise direction near the leading edge, but they progressively become three-dimensional.

**4.2. Aeroacoustics results**

To confirm the accuracy of the acoustic simulation, the sound pressure level (SPL) is compared with the existing experimental results of Brooks et al. [5]. The airfoil chord and span used in the experiment were 5.08 and 45.72 cm, respectively. The acoustic measurements were conducted with a set of eight microphones. The sound pressure level (SPL) for an observer at 1.22 m on top of the trailing edge is reported in terms of one-third octave.

In the present computation, a small portion of the actual span of Brooks et al.'s experiment [5] is simulated. The span ratio is  $\frac{L_z-Exp}{L_z-LES} = 90$  which means the whole airfoil consist of 90 source regions. The simplest way is to assume that the sound pressure fluctuations have the same intensity and phase angle in every source region along the span [26]. Therefore, the total noise from the entire span is the sum of contributions of 90 independent source regions along the span. This assumption leads to an over prediction of the sound pressure level as observed in [22]. Figure 11 presents a comparison of third-octave sound pressure level as a function of frequency between the current simulation and the experiment.

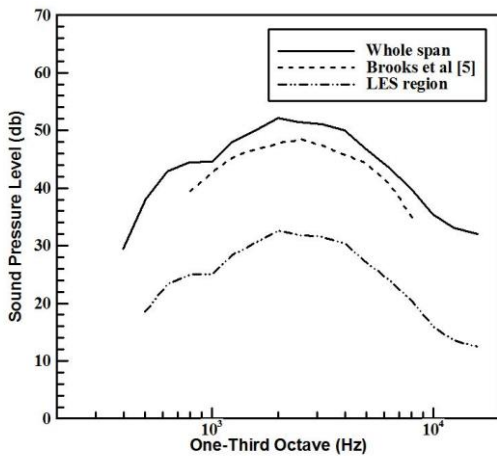


Fig. 11. Comparison of SPL in third-octave bands at 1.22 m from NACA 0012 airfoil [5]

It can be observed that there is good agreement between LES and the experimental data.

It is generally known that the sound pressure level at the receiver location is highly dependent on the distance between the receiver and the noise source. This effect is shown in Figure 12 where the sound pressure level is computed on the top of the trailing edge at different distances,  $D= 12c, 24c$  and  $48c$ . It can be observed that the noise peak that occurs at  $f= 2000Hz$  matches with the peak frequency in the lift power spectral density.

The effect of receiver location on the overall sound pressure level (OASPL) is shown in Figure 13. The OASPL is evaluated by integration over the frequency spectrum.

It can be seen that the OASPL does not vary linearly with the receiver distance. This means that doubling the receiver distance does not mean halving the sound pressure level. The OASPL varies logarithmically with the receiver distance to the airfoil.

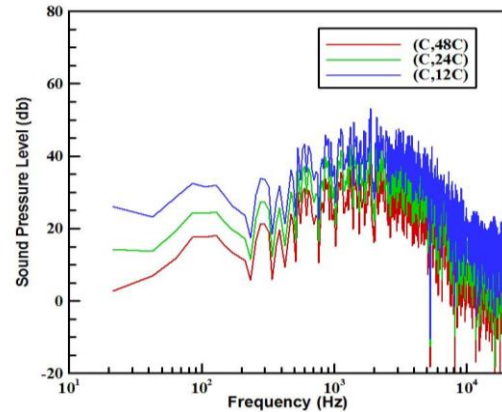


Fig. 12. Sound pressure level vs. frequency at receivers located top trailing edge at different distances

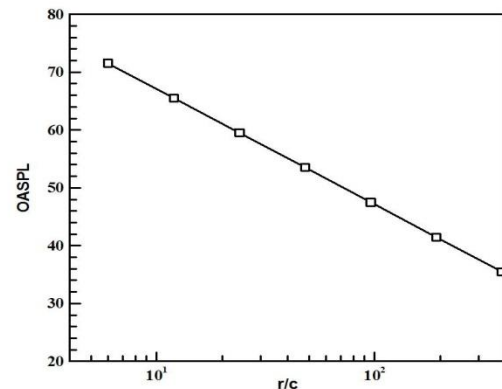


Fig. 13. The overall sound pressure level at different distances from the airfoil

## 5. Conclusions

A series of large eddy simulations have been carried out for the laminar and turbulent boundary layer flows passing a NACA 0012 airfoil at  $Re=100,000$  and  $AoA=8.4\text{deg}$ . Both mean flow quantities and fluctuation statistics were studied. The computed non-dimensional mean velocity profiles in the boundary layer compared reasonably well with the theoretical predictions. The skin friction coefficient and the  $u_{rms}$  streamwise velocity fluctuations predicted a transition zone from  $x/c=0.23$  to  $x/c=0.45$ . Lift power spectral density was studied and its behaviour was related to boundary layer developing phenomena such as laminar boundary vortex shedding.

The far-field acoustic prediction was performed by the Ffowcs Williams and Hawkings (FW-H) acoustic analogy. The surface pressure fluctuations were used as the acoustic source field data and they were converted to the frequency domain using Fast Fourier Transform (FFT). It was assumed that sound pressure fluctuations have the same intensity and phase angle in every source region along the airfoil span. Therefore, the total noise from the entire span is the sum of contributions of 90 independent source regions along the span. The spectra computed from the pressure field agree well with the experimental measurement at the same observer location. Also, the effect of receiver location on the overall sound pressure level (OASPL) was studied and it was observed that OASPL varies logarithmically with the receiver distance.

## References

- [1]. Jianu, O., Rosen, M. A., and Naterer, G., 2012, "Noise Pollution Prevention in Wind Turbines: Status and Recent Advances," *Sustainability*, **4**(6): 1104-1117.
- [2]. Pedersen, E., and Waye, K. P., 2007, "Wind turbine noise, annoyance and self-reported health and well-being in different living environments," *Occupational and environmental medicine*, **64**(7): 480-486.
- [3]. Wagner, S., Bareiss, R., Guidati, G., and Wagner-Bareiß-Guidati, 1996, "Wind turbine noise."
- [4]. Oerlemans, S., Sijtsma, P., and Méndez López, B., 2007, "Location and quantification of noise sources on a wind turbine," *Journal of sound and vibration*, **299**(4): 869-883.
- [5]. Brooks, T. F., Pope, D. S., and Marcolini, M. A., 1989, *Airfoil self-noise and prediction*, National Aeronautics and Space Administration, Office of Management, Scientific and Technical Information Division.
- [6]. Wang, M., and Moin, P., 2000, "Computation of trailing-edge flow and noise using large-eddy simulation," *AIAA journal*, **38**(12): 2201-2209.
- [7]. Williams, J., and Hall, L., 1970, "Aerodynamic sound generation by turbulent flow in the vicinity of a scattering half plane," *Journal of Fluid Mechanics*, **40**(04): 657-670.
- [8]. Singer, B. A., Brentner, K. S., Lockard, D. P., and Lilley, G. M., 2000, "Simulation of acoustic scattering from a trailing edge," *Journal of Sound and Vibration*, **230**(3): 541-560.
- [9]. Shen, W. Z., Zhu, W., and Sørensen, J. N., 2009, "Aeroacoustic computations for turbulent airfoil flows," *AIAA journal*, **47**(6): 1518-1527.
- [10]. Jones, L. E., Sandham, N. D., and Sandberg, R. D., 2010, "Acoustic source identification for transitional airfoil flows using cross correlations," *AIAA journal*, **48**(10): 2299-2312.
- [11]. Kim, T., Lee, S., Kim, H., and Lee, S., 2010, "Design of low noise airfoil with high aerodynamic performance for use on small wind turbines," *Science in China Series E: Technological Sciences*, **53**(1): 75-79.
- [12]. Göçmen, T., and Özerdem, B., 2012, "Airfoil optimization for noise emission problem and aerodynamic performance criterion on small scale wind turbines," *Energy*, **46**(1): 62-71.
- [13]. Wolf, W. R., and Lele, S. K., 2012, "Trailing-Edge Noise Predictions Using Compressible Large-Eddy Simulation and Acoustic Analogy," *AIAA journal*, **50**(11): 2423-2434.
- [14]. Lilly, D. K., 1992, "A proposed modification of the Germano subgrid-scale closure method," *Physics of Fluids A: Fluid Dynamics (1989-1993)*, **4**(3): 633-635.
- [15]. Williams, J. F., and Hawkings, D. L., 1969, "Sound generation by turbulence and surfaces in arbitrary motion," *Philosophical Transactions of the Royal Society of London. Series A, Mathematical and Physical Sciences*, **264**(1151): 321-342.
- [16]. Lighthill, M. J., 1952, "On sound generated aerodynamically. I. General theory," *Proceedings of the Royal Society of London. Series A. Mathematical and Physical Sciences*, **211**(1107): 564-587.
- [17]. Di Francescantonio, P., 1997, "A new boundary integral formulation for the prediction of sound radiation," *Journal of Sound and Vibration*, **202**(4): 491-509.
- [18]. Morris, P. J., Long, L. N., and Brentner, K. S., "An aeroacoustic analysis of wind turbines," *Proc. 23rd ASME Wind Energy Symposium*, AIAA Paper: 5-8.

- [19]. Farassat, F., and Succi, G. P., "The prediction of helicopter rotor discrete frequency noise," Proc. In: American Helicopter Society, Annual Forum, 38th, Anaheim, CA, May 4-7, 1982, Proceedings.(A82-40505 20-01) Washington, DC, American Helicopter Society, 1982: 497-507.
- [20]. Sheldahl, R. E., and Klimas, P. C., 1981, "Aerodynamic characteristics of seven symmetrical airfoil sections through 180-degree angle of attack for use in aerodynamic analysis of vertical axis wind turbines," Sandia National Labs., Albuquerque, NM (USA).
- [21]. Afzal, N., "Wake layer in a turbulent boundary layer with pressure gradient- A new approach," Proc. IUTAM Symposium on Asymptotic Methods for Turbulent Shear Flows at High Reynolds Numbers, Bochum, Germany: 95-118.
- [22]. Marsden, O., Bogey, C., and Bailly, C., 2008, "Direct noise computation of the turbulent flow around a zero-incidence airfoil," *AIAA journal*, **46**(4): 874-883.
- [23]. Hoffmann, J. A., Kassir, S., and Larwood, S., 1989, "The influence of free-stream turbulence on turbulent boundary layers with mild adverse pressure gradients."
- [24]. Hunt, J. C., Wray, A., and Moin, P., "Eddies, streams, and convergence zones in turbulent flows," Proc. Studying Turbulence Using Numerical Simulation Databases, **2**: 193-208.
- [25]. Chakraborty, P., Balachandar, S., and Adrian, R. J., 2005, "On the relationships between local vortex identification schemes," *Journal of Fluid Mechanics*, **535**: 189-214.
- [26]. Kato, C., Iida, A., Takano, Y., Fujita, H., and Ikegawa, M., 1993, "Numerical prediction of aerodynamic noise radiated from low mach number turbulent wake," *AIAA paper*(93-0145).